Applied Surface Science 509 (2020) 144822

Contents lists available at ScienceDirect

Applied Surface Science

journal homepage: www.elsevier.com/locate/apsusc

Full Length Article

Layer-dependent dielectric permittivity of topological insulator Bi_2Se_3 thin films

Mingsheng Fang[a,1], Zhengyu Wang[c,d,1], Honggang Gu[a,1,*], Mingyu Tong[b], Baokun Song[a], Xiangnan Xie[e], Tong Zhou[e], Xiuguo Chen[a], Hao Jiang[a], Tian Jiang[b,*], Shiyuan Liu[a,*]

[a] State Key Laboratory of Digital Manufacturing Equipment and Technology, Huazhong University of Science and Technology, Wuhan, 430074, PR China
[b] College of Advanced Interdisciplinary Studies, National University of Defense Technology, Changsha 410073, PR China
[c] National Innovation Institute of Defense Technology, Academy of Military Sciences PLA China, Beijing 100010, PR China
[d] Beijing Academy of Quantum Information Sciences, Beijing 100084, PR China
[e] State Key Laboratory of High Performance Computing, College of Computer, National University of Defense Technology, Changsha 410073, PR China

ARTICLE INFO

Keywords:
Bi_2Se_3 thin films
Layer-dependent dielectric permittivity
Hybridization
Joint density of states
Spectroscopic ellipsometry

ABSTRACT

Dielectric properties and their evolutions are fundamental to reveal the optical responses of topological insulators and to guide the design of related devices. Here, we systematically investigate the layer-dependent dielectric permittivity of Bi_2Se_3 over an ultra-broad spectral range (0.73–6.43 eV) by combining the spectroscopic ellipsometry, energy-loss function (ELF), critical point (CP) analysis, and density function theory. Results demonstrate that the epsilon-near-zero point of the real permittivity and the ELF peak exhibit blue shifts, indicating the resonance frequencies of surface plasmon modes move towards the higher energy, due to the enhanced hybridization between the opposite surfaces. The joint density of states dominates the layer-dependent increase in imaginary permittivity as the thickness increases. We also find that the CP transition positions in band structures are layer-independent, and the CP center energies exhibit red shifts resulted by the reduced surface state gap with the thickness increasing.

1. Introduction

Since the first experimental demonstration of two-dimensional (2D) topological insulators (TIs) HgCdTe quantum well structures in 2007, and subsequent discovery of 3D TIs, including Bi_2Te_3, Bi_2Se_3 and Sb_2Te_3, researches on TIs have expanded remarkably [1]. Different from normal insulators, in the TIs, a bulk bandgap opens due to the strong spin-orbit interactions while their edge or surface states are metallic [2-4]. Recently, TIs have been demonstrated as novel plasmonic materials both from a fundamental physics perspective, as they are expected to exhibit varieties of plasmons in the topological surface states, and from a device perspective, as they have plasmonic resonances from terahertz to ultraviolet range [5-7]. In 3D TIs, the surface states are topologically protected by time-reversal symmetry, and hence robust against weak perturbation or disorder, which gives rise to some unique properties, such as the saturable-absorption [8], nonlocal transports [9], spin-momentum locking [10], unconventional superconductivities [11], and Majorana fermions [12]. These unique properties make 3D TIs ideal for applications in saturable absorber [13], planar devices [14], low-power spintronics [15], topological quantum computing [11], and flexible electrodes [16].

The bismuth selenide (Bi_2Se_3), as a representative of 3D TIs, has gained great attentions due to the wide bulk bandgap and the single Dirac cone on the surface [17-19]. It belongs to a strong TI and has a large bulk bandgap of ~0.3 eV [1]. The electronic band structures were studied by first-principles calculations and a single Dirac cone was observed at Γ point in the center of Brillouin zone by angle-resolved photoelectron spectroscopy (ARPES) measurements [18,19]. Bi_2Se_3 has a layered structure consisting of quintuple layers (QLs) with weak van der Waals force among adjacent QLs, which makes it easy to obtain layer-controllable thin films [20]. The molecular beam epitaxy (MBE) and nanoribbon growth methods have been widely employed to prepare high-quality Bi_2Se_3 thin films [21,22]. The Bi_2Se_3 thin film will experience a dimensional crossover from nontrivial 3D TI to trivial insulator at 6 QLs [23-26], which means as the thickness approaches the two dimensional limit (< 6QL), a finite bandgap opens in the surface states of the Bi_2Se_3 thin film due to the hybridization between the bottom and top surface states (i.e., the finite-size effects). In addition,

* Corresponding authors.
E-mail addresses: hongganggu@hust.edu.cn (H. Gu), tjiang@nudt.edu.cn (T. Jiang), shyliu@hust.edu.cn (S. Liu).
[1] These authors contributed equally to this work.

https://doi.org/10.1016/j.apsusc.2019.144822
Received 15 October 2019; Received in revised form 18 November 2019; Accepted 20 November 2019
Available online 29 November 2019

Bi_2Se_3 is of great potential for device applications among currently known TIs, and recently the two dimensional Bi_2Se_3 thin films have shown promising optoelectronic functionality in photodetector and optoelectronic devices [27-30].

The optical properties of Bi_2Se_3 thin films are the basis for related optoelectronic applications. As an essential optical property, the dielectric permittivity describes the propagation and loss of the electromagnetic wave in the medium, which reflects light–matter interactions. For example, the epsilon-near-zero (ENZ) points in the real part of permittivity are related to the surface plasmon modes in TIs, and the ENZ photonics has been an important research field in recent years [31-34]. Meanwhile, the imaginary part of permittivity indicates the optical absorption and optical transitions, etc [35-37]. Therefore, the accurate and quantitative characterization of the permittivity for Bi_2Se_3 thin films is of great importance to reveal the physical origins of optical responses and to guide the optimal design and performance improvement of related optoelectronic devices. There have been some researches focusing on the permittivity of Bi_2Se_3 thin films. Eddrief et al. measured the permittivity of 3–54 QL Bi_2Se_3 thin films and found a blue shift at the maximum absorption band near 2 eV while the thickness is reduced below 19 QLs [38]. Sapkota et al. reported the absorption spectra and dielectric constants of 2–10 nm Bi_2Se_3 thin films and provided direct optical evidence for the blue shift in the bulk bandgap of Bi_2Se_3 as the thickness approaches the two-dimensional limit [39]. Li et al. predicted the dielectric properties of 1–8 QL Bi_2Se_3 by theoretical calculations and discovered the coupling interactions between the bottom and top surface states that result in red and blue shifts of the multiple-peak structures of the imaginary permittivity as the thickness increased [40]. However, a systematic investigation on the permittivity of Bi_2Se_3 and their layer-dependent evolutions is still lacking at the two-dimensional limit. Especially, published studies rarely discussed the layer dependent ENZ properties and the critical points (CPs) in the permittivity and further revealed their physical essences related to the light–matter interactions of Bi_2Se_3. In this work, by utilizing the energy-loss function (ELF) analysis and CP analysis, we investigate, for the first time, the hybridization and joint density of states (JDOS) induced evolutions in the permittivity of 2–10 QL Bi_2Se_3 via spectroscopic ellipsometry (SE) combining with the density function theory (DFT) calculations.

High-quality, strictly layer-controllable, atomically flat and large area (centimeter) Bi_2Se_3 thin films are fabricated by the MBE method. The permittivity of 2–10 QL Bi_2Se_3 thin films are determined by the SE over an ultra-broad spectral range (0.73–6.43 eV), and further the ELF is extracted and discussed. By using the CP analysis, up to five CPs are precisely identified in the permittivity spectra. Moreover, the band structures, partial density of states (PDOS) and the theoretical permittivity of 2–10 QL Bi_2Se_3 are calculated by the DFT. By comparing these experimental and theoretical results, our studies revealed that the ENZ point in the real part of permittivity and the energy-loss peak in the ELF exhibit obvious blue shifts due to the hybridization-induced surface state gap as the thickness approaches two-dimensional limits. With the QL increasing, the JDOS dominates the layer-dependent increase in the imaginary part of permittivity. Additionally, results confirm that the transition positions of the CPs in band structures are layer-independent, and the CP center energies exhibit red shifts as the QL increases, which are caused by the decreased surface state gap due to the attenuated hybridization between the opposite surfaces.

2. Sample preparation and characterization

2.1. Bi_2Se_3 thin films preparation

Centimeter-scale Bi_2Se_3 thin films with variable thickness (2, 4, 6, 8, and 10 QLs) were prepared by the molecular beam epitaxy (MBE). The MBE growth was performed in a custom-made MBE system with a base pressure of $\sim 1 \times 10^{-10}$ Torr. The sapphire (Al_2O_3) is chosen as the substrate, which was prepared by heating to 600 °C for 2 h and 800 °C for 1 h by indirect heating in the MBE chamber. High-purity elemental Bi (99.999%) and Se (99.999%) were thermally evaporated from standard Knusden cells. The Bi flux was calibrated by measuring the thickness of as-grown Bi_2Se_3 thin films using scanning tunneling microscopy (STM) and atomic force microscope (AFM). To ensure stoichiometric samples were grown, a high Se/Bi flux radio (greater than 15) was used, while the substrate temperature was kept around 200 °C measured by an infrared pyrometer. All MBE growth was followed by 10 min of annealing, with growth temperature maintained and all evaporators shut off [26,41].

2.2. Characterization of Bi_2Se_3 thin films

In order to demonstrate the successful growth of Bi_2Se_3 thin films, the RH30OM reflection high-energy electric diffraction (RHEED) measurement system was used to demonstrate the high crystal quality of the samples. And the purities of Bi_2Se_3 thin film were examined by Raman spectrometer (inVia reflex, RENISHAW). The surface conditions of Bi_2Se_3 thin films were checked by an optical microscope (OM) and the surface roughness was determined by an atomic force microscopy (AFM) (Bruker Dimension Icon). Besides, the thicknesses of the Bi_2Se_3 thin films were measured by the AFM and a high resolution transmission electron microscope (HRTEM) system (FEI Tian G2-300).

2.3. Ellipsometry measurements

Centimeter-scale 2–10 QL Bi_2Se_3 thin films were investigated by a commercial dual rotating-compensator spectroscopic ellipsometer (M-L Muller matrix ellpsometer, Wuhan Eoptics Technology Co., Wuhan, China) within the air ambient. The data on Bi_2Se_3 thin films was gathered over an ultra-broad spectral range of 0.73–6.42 eV, and the diameter of the probing spot can be as small as 200 μm by using a pair of focusing probes. The multi-incidence measurement mode was used to reduce the correlations among the variables to be determined, and the incident angles were set at 60°, 65° and 70°.

3. Density functional theory (DFT) calculation

For the Bi_2Se_3 unit cell, the experimental lattice constants ($a = b = 4.138$ Å and $c = 28.640$ Å) were used to build this hexagonal unit cell [42]. In the 2–10 QL Bi_2Se_3 models, the slabs in the adjacent unit cells were separated by a vacuum of 18 Å. All calculations were performed with Vienna ab *initio* package (VASP). The exchange correlation potential was approximated by the generalized gradient approximation with Perdew-Burke-Ernzerhopf (PBE) functional based on projector-augmented-wave (PAW) pseudopotentials [43]. In order to consider the van der Waals interaction, optimized Perdew-Burke-Ernzerhof-vdW (optPBE-vdW) method was taken into consideration because it appears to be a better function for Bi_2Se_3 [44].

In geometric optimization, the structures were optimized with PBE functional based on PAW pseudopotentials, and the kinetic energy cutoff was set at 500 eV and Brillouin zone was sampled with a $10 \times 10 \times 1$ Γ-centered *k*-point mesh. The criterion for the convergence of forces and total energy were set to 0.01 eV/Å and 10^{-5} eV. In the band structures and PDOS calculations, the PBE functional based on PAW pseudopotentials was also used, the kinetic energy cutoff was set at 500 eV and the Brillouin zone sampled with a $12 \times 12 \times 1$ Γ-centered *k*-point mesh. The dielectric permittivity was calculated based on the electronic ground states and a strict electronic convergence criterion of 10^{-8} was used to ensure accuracy. All these calculations included spin–orbit coupling (SOC).

4. Results and discussion

Bi_2Se_3 belongs to the rhombohedral crystal structure with the space

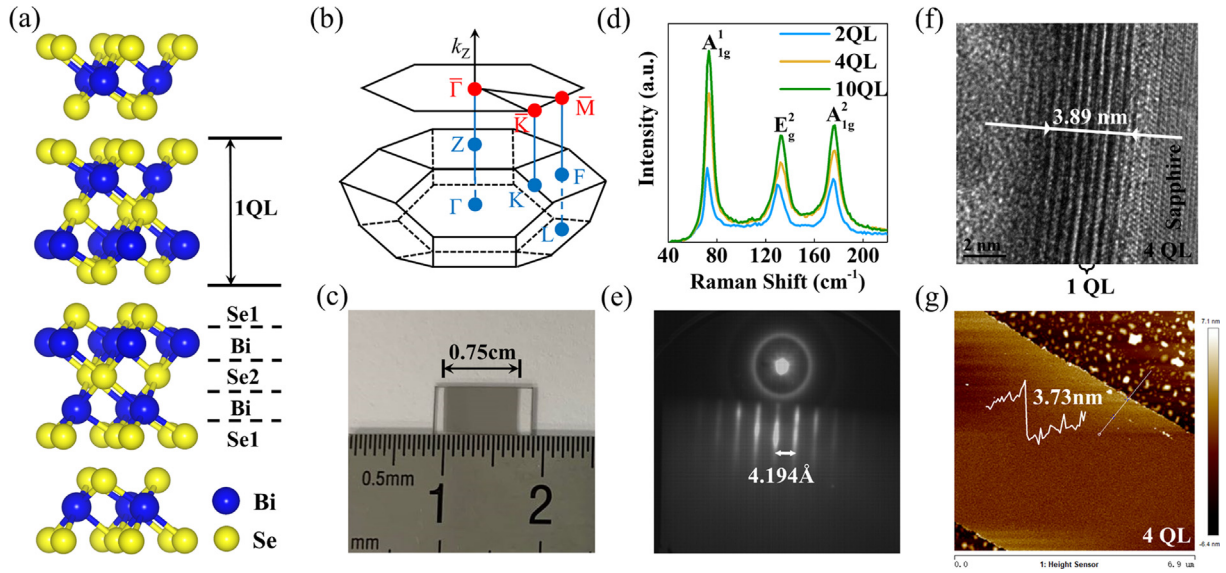

Fig. 1. (a) The hexagonal supercell of Bi_2Se_3, with five atomic layers of Se1-Bi-Se2-Bi-Se1 forming a QL. (b) The bulk and the projected (1 1 1) Brillouin zones. (c) Optical picture of 10-QL Bi_2Se_3 thin films on the sapphire substrate. (d) Raman spectra of 2-QL, 4-QL and 10-QL Bi_2Se_3 thin films. (e) The RHEED patterns of Bi_2Se_3 (f) HRTEM image of 4-QL Bi_2Se_3 thin film. (g) AFM morphology image of a typical 4-QL Bi_2Se_3 thin films.

group $D^5_{3d}(R\bar{3}m)$ [42], as schematically shown in Fig. 1(a). Along the [1 1 1] crystallographic direction, the layered structure is stacked with periodic five atomic layers (Se1-Bi-Se2-Bi-Se1), denoted as a quintuple layer (QL), and the hexagonal primitive cell spans three QLs. The covalent bonds dominate the bonding within a QL, whereas the van der Waals forces dominate the bonding between QLs [18]. The bulk and projected (1 1 1) Brillouin zones are showed in Fig. 1(b), and the electronic band structures of Bi_2Se_3 thin films are calculated along the relevant $\bar{K}-\bar{\Gamma}-\bar{M}-\bar{K}$ branches in the projected (1 1 1) Brillouin zones. Fig. 1(c) shows the representative optical picture of 10-QL Bi_2Se_3 thin film on the sapphire substrate, where the Bi_2Se_3 thin film has a domain size of 0.75 cm. The crystalline qualities of the Bi_2Se_3 thin films are characterized by Raman spectra and RHEED, as presented in Fig. 1(d–e). The Raman spectra in Fig. 1(d) show three intensity peaks (A^1_{1g}, E^2_g, A^2_{1g}) around 73.4 cm^{-1}, 132.1 cm^{-1}, and 176.9 cm^{-1} respectively, consistent with previous reports [41,45]. The RHEED patterns in Fig. 1(e) indicate that the lattice constant of Bi_2Se_3 thin films on sapphire substrate is 4.194 Å, in agreement with the previously reported values [24,41]. Furthermore, the thicknesses and the surface conditions of Bi_2Se_3 thin films are detected by the HRTEM and AFM. As shown in Fig. 1(f), the HRTEM image of the 4-QL Bi_2Se_3 thin film reveals the clear stratified structure with 4 QLs, whose thickness is 3.89 nm. Fig. 1(e) and Fig. S2 present the AFM results of 4-QL, 8-QL and 10-QL Bi_2Se_3 thin films, respectively. It is clear that these Bi_2Se_3 thin films have extremely low roughness values (Rq) and the thicknesses are 3.73 nm, 7.96 nm and 9.17 nm, respectively. All these characterizations demonstrate that the Bi_2Se_3 thin films in our experiments are large-area, high-quality, strictly layer-controlled and atomically flat, which will benefit us a lot to perform the ellipsometry investigation.

The Bi_2Se_3 thin films with different QLs were investigated by the dual rotating-compensator spectroscopic ellipsometer, as illustrated in Fig. 2(a–b) [46,47]. Fig. 2(a) shows the principle diagram of spectroscopic ellipsometry (SE) measurements, and Fig. 2(b) presents the commercial ellipsometer (ME-L Muller matrix ellipsometer, Wuhan Eoptics Technology Co., Wuhan, China) we used. Ellipsometry is a widely used optical technique for the characterization of nanomaterials and nanostructures by detecting the polarization state change of the polarized light after reacting with the samples [48,49]. The polarization state change is usually described by two ellipsometric angles (Ψ, Δ) in the SE, which can be defined with the reflection coefficients according to

$$r_p/r_s = |r_p/r_s|\cdot e^{i(\delta_p-\delta_s)} = \tan(\psi)\cdot e^{i\Delta}, \quad (1)$$

wherein, r_p and r_s are the reflection coefficients for the p-polarization and the s-polarization respectively, $|r_p/r_s|$ represents the amplitude ratio between p- and s-polarizations, and δ_p and δ_s refer to the phase shifts of p- and s-polarizations respectively. From the optical microscope (OM) images as shown in Fig. S1, we can see that the Bi_2Se_3 thin film samples have a fairly smooth surface over large area, which are suitable for ellipsometric measurements. In this work, the ellipsometric data of Bi_2Se_3 thin films was recorded over the spectral range of 0.73–6.42 eV with the incidence (θ) ranging from 60° to 70° in steps of 5°.

The SE is a model-based technique, and to determine the permittivity of Bi_2Se_3 thin films, an optical model should be constructed to fit the measured ellipsometic spectra. According to the previous studies [38,39], oxidation and other extrinsic effects in Bi_2Se_3 thin films do not dominate the SE measurements. Besides, the above-mentioned AFM and OM results show that our MBE-grown Bi_2Se_3 thin films have an extremely smooth surface. So in the ellipsometric fitting, the oxide layer and surface roughness were not taken into consideration and a three-layer stacking model (ambient/Bi_2Se_3/c-sapphire) was constructed to describe the optical structure of the Bi_2Se_3 thin films on sapphire substrate. The permittivity of Bi_2Se_3 is described by a parameterized dispersive model consisting of five Lorentz oscillators and two Gaussian oscillators [50-52]. With the constructed optical dielectric and dielectric model, the theoretical ellipsometric spectra ($\Psi(E)$, $\Delta(E)$) of the Bi_2Se_3 thin films can be calculated by the transfer matrix method [50]. Then the measured ellipsometric spectra were fitted by theoretically calculated ones with Levenberg–Marquardt algorithm by minimizing the Mean Squared Error (MSE) as given by

$$MSE = \sqrt{\sum_{i=1}^{n}\left[(\tan\psi_i^{fit}) - (\tan\psi_i^{measured})^2 + (\cos\Delta_i^{fit} - \cos\Delta_i^{measured})^2\right]}, \quad (2)$$

where n and m represent the numbers of the measurement data and the variables to be fitted, respectively. From the viewpoint of mathematics, the lower MSE indicates the better agreement between the theoretical and measured spectra. Fig. 3 shows measured (open circles) and best-fitting (solid lines) ellipsometric spectra of ($\Psi(E)$, $\Delta(E)$). It can be seen from Fig. 3 that the theoretical spectra present fairly agreement with the measured ones. The fitting MSE values of 2–10 QL Bi_2Se_3 thin films

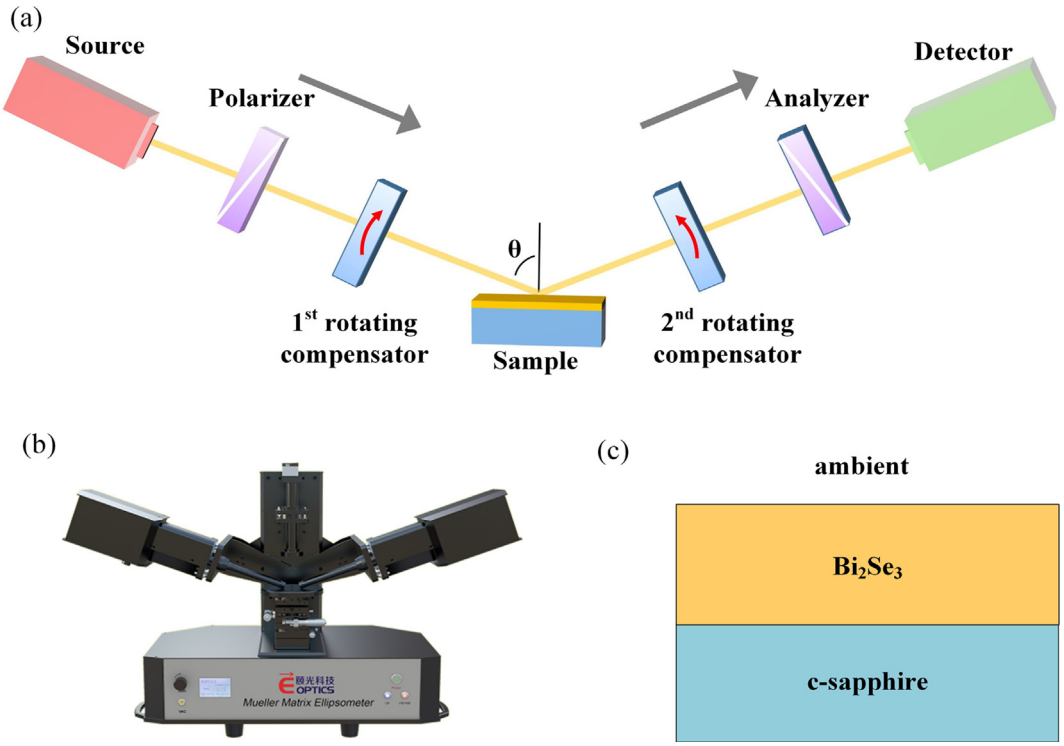

Fig. 2. (a) Schematic illustration of spectrometric ellipsometry measurements of Bi_2Se_3 thin film. (b) A photograph of the experimental SE set-up. (c) The constructed optical model of the Bi_2Se_3 thin film in ellipsometric fitting.

are 3.205, 2.933, 3.142, 4.426 and 3.309 respectively, which are relatively low level of well-fitting ellipsometric analysis. In addition, the thicknesses obtained by the SE fittings are consistent with AFM/HRTEM results and the theoretical values, as summarized in Table S1.

Fig. 4(a–b) illustrates the dielectric permittivity ($\varepsilon_r + i\varepsilon_i$) of Bi_2Se_3 thin films with different QLs obtained by the SE. Compared to previous publications [38,39], our results are more systematic with the thickness ranging from 2 QLs to 10 QLs, and cover a much broader spectral range (0.73–6.43 eV), which will be beneficial for us to comprehensively investigate the optical properties of Bi_2Se_3 thin films. In this work, the DFT calculations are also performed on the Bi_2Se_3 thin films with different QLs, and the calculated permittivity is illustrated in Fig. S4, which agrees well with the experimental results obtained by the SE.

Dielectric permittivity is one of the most important parameters pertaining to the surface plasmons in TIs. To support surface plasmons at the interface between the metallic surface and the dielectric layer, the real part (ε_r) of permittivity should be negative [53]. As shown in Fig. 4(a), ε_r becomes negative when the photon energy is greater than the epsilon-near-zero (ENZ) point (E_{ENZ}, where $\varepsilon_r = 0$), which suggests that the surface plasmons of Bi_2Se_3 thin films have resonant frequencies greater than E_{ENZ}. Therefore, the ENZ point (E_{ENZ}) can be regarded as a reference for surface plasmon modes [34,54,55]. Fig. 4(a) demonstrates that when the QL is larger than 6, E_{ENZ} remains nearly unchanged. While the QL decreases from 6 to 2, E_{ENZ} exhibits an obvious blue shift from 2.30 eV to 3.12 eV, suggesting that the surface plasmon modes of Bi_2Se_3 could have gradually changed. The similar blue-shifted trend for the ENZ point can be also found from the DFT results shown in Fig. S4(a). To further confirm the changes of the surface plasmon modes, we derive the energy-loss function (ELF) from the permittivity:

$$E = \mathrm{Im}\left(\frac{-1}{\varepsilon}\right) = \frac{\varepsilon_i}{\varepsilon_r^2 + \varepsilon_i^2}, \quad (3)$$

The ELF illustrated in Fig. 4(c) describes the spectra density of the intrinsic plasmontic excitation [56]. The ELF spectrum presents a weak energy-loss peak E_S, indicating that a surface plasmon mode could exist at the E_S position. It can be observed that E_S shifts to the higher energy direction when the thickness of Bi_2Se_3 approaches the two-dimensional limit, which is intuitively presented in Fig. 4(d). Specifically, when the QL is greater than 6, E_S is basically unchanged. But when the QL decreases from 6 to 2, E_S exhibits a slight blue shift from 3.36 eV to 3.47 eV. The evolutions in both the ε_r and the ELF indicate the resonance frequencies of surface plasmon modes gradually move toward the higher energy. We propose that when the thickness of Bi_2Se_3 is thicker than 6 QLs [26], the hybridization between the opposite surfaces doesn't exist and the surface plasmon modes remain unchanged, leading to no shift in E_{ENZ} and E_S. While the thickness of Bi_2Se_3 becomes thinner than 6 QLs [26], the hybridization between the opposite surfaces leads to the increase of the surface state gap [23,24,26], and then the frequencies of surface plasmon modes shift to higher energy direction, which finally results in the blue-shifted E_{ENZ} and E_S.

As shown in Fig. 4(b), there exist five CPs (labeled with uppercase letters A–E) in the imaginary part (ε_i) of permittivity of Bi_2Se_3 thin films over the concerned spectral range. As the thickness increases, the magnitude of ε_i increases, but the increment rate is gradually reduced. Additionally, the energy positions of the CPs present red shifts, and two shoulder CPs C and D gradually combine into one wide peak, namely the main peak in the spectra of ε_i, and their energy positions gradually approach to each other with the QL increasing. In order to quantitatively identify and analyze the feature peaks, the CP analysis method is applied, and the details about the process and results are given in Supplementary Material (Fig. S3 and Table S2). Based on the CP analysis, the center energies and the dimensionalities of the CPs can be precisely determined. The second derivative of the permittivity spectra are best fitted by CPs with dimensionality $n = -1$, indicating the optical transitions at all these CPs contain excitonic effects. In order to further analyze the obvious layer-dependent dielectric properties of Bi_2Se_3, the center energies of the CPs and the magnitudes of ε_i at these CPs versus the QL are illustrated in Fig. 5. From Fig. 5(a), we can see that the center energies of all these five CPs present slight red shifts (about 0.17–0.33 eV) with the QL number increasing from 2 to 6. While

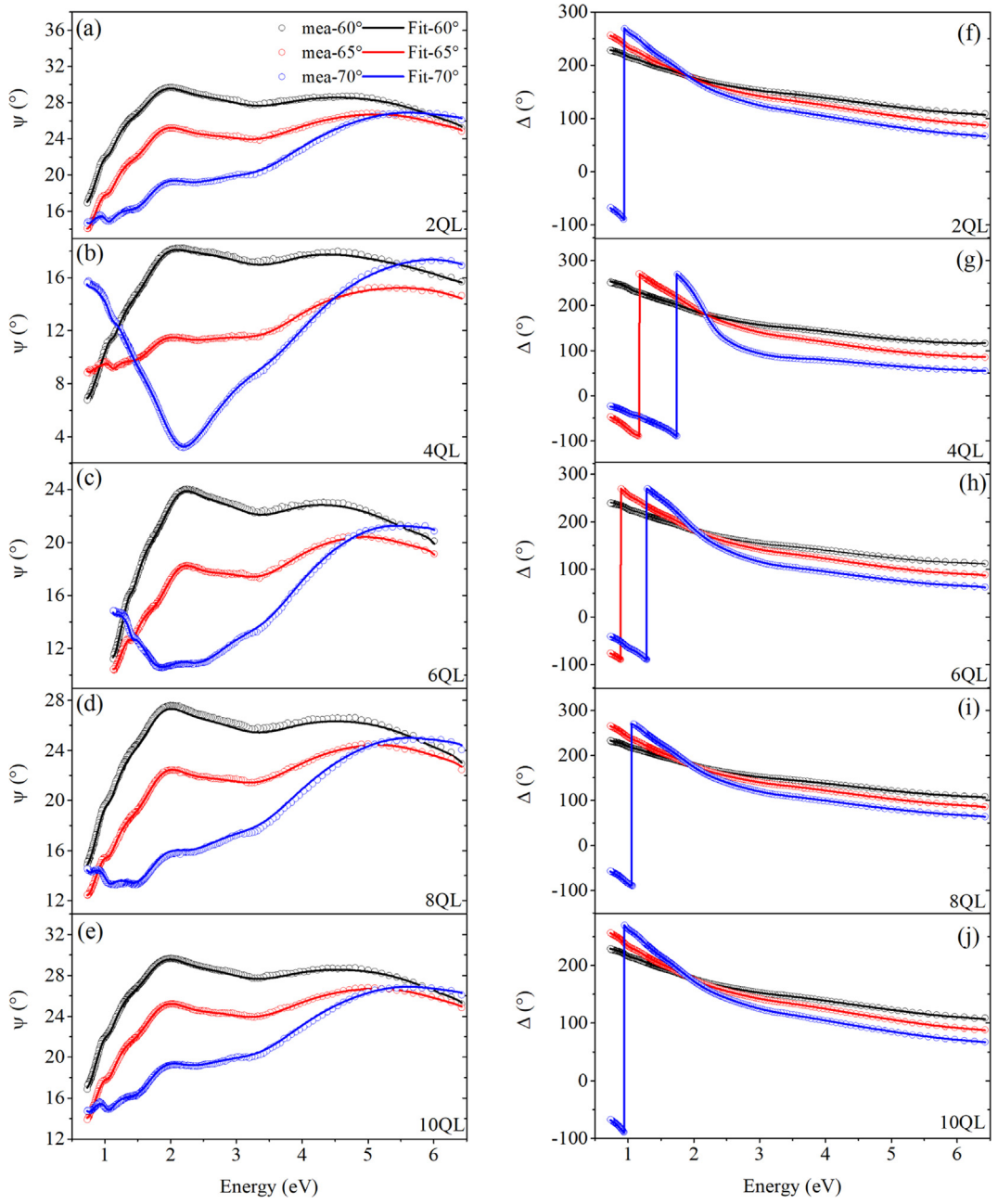

Fig. 3. Experimental and fitted Psi (Ψ) and Delta (Δ) for the 2–10 QL Bi_2Se_3 thin films on sapphire substrate for incident angle of 60, 65 and 70°.

the QL is larger than 6, the center energies of these CPs nearly remain unchanged. Besides, Fig. 5(b) clearly shows that the magnitudes of ε_i at CPs A–D increase but the increment rates gradually decrease when the thickness changes from 2 QLs to 6 QLs. As the thickness reaches over 6 QLs, the increment in ε_i can be neglected. Differently, as for CP E, the magnitude of ε_i is nearly unchanged with the QL.

In view of the microscopic theory, the imaginary part of permittivity is basically related to three effects: the optical matrix element, the joint density of states (JDOS) and the excitonic effects [57]. The optical matrix element is independent on geometric features at quantum wells [58]. Since the 2–10 QL Bi_2Se_3 thin films can be treated as quantum wells, the optical matrix element can be taken as a constant. Therefore, the imaginary part of the permittivity of the Bi_2Se_3 thin film is decided by the JDOS and the excitonic effects. The JDOS is related to the valence and conduction band states involved in the optical transition, which is determined by the band structure in the *k*-space and promised to monotonically increase with the thickness [57,59]. The excitonic effects present the electron-hole interactions on the permittivity, which can increase the magnitude of ε_i. The strength of the excitonic effect is expected to quickly decrease with the thickness [57,59].

To qualitatively analyze the impact of the JDOS and the excitonic effects on the evolutions of the imaginary part of permittivity, the SE measured ε_i-QL curves are compared with the DFT calculated ones. In the DFT calculations, we deliberately only take the JDOS effects into consideration [60], so that the impact of the JDOS and the excitonic effects can be distinguished by comparing experimental and calculated results. Here, we take CP C with the maximum magnitude of ε_i as a representative in the following discussions, as illustrated in Fig. 5(c). The calculated ε_i-QL curve shows that the JDOS will increase when the film thickness increases from 2 QLs to 6 QLs, but accompanied by a reduced increment rate. When the QL is larger than 6, the increment becomes extremely weak and thus can be neglected. This is because the film gradually approaches the three-dimensional scale. It can be seen that the experimental results exhibit similar evolution trends with the

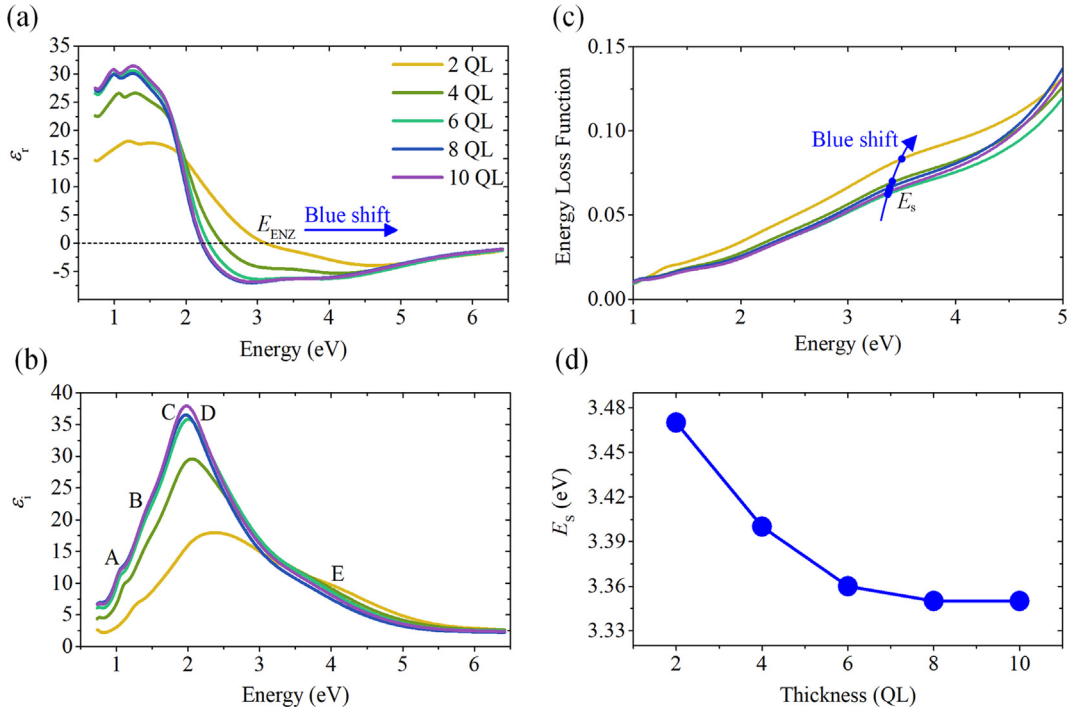

Fig. 4. (a) Real part of permittivity of Bi_2Se_3 thin films with different QLs. E_{ENZ} tags the epsilon-near zero (ENZ) point where $\varepsilon_r = 0$. (b) Imaginary part of permittivity, 5 CPs are labeled with A–E. (c) Energy Loss Functions, the weak energy-loss peaks (E_S) are marked with blue solid dots. (d) The energy positions of E_S versus the QL number.

calculated results, but with larger magnitudes. This similar evolution trends demonstrate that the JDOS is the dominant factor for the layer-dependent evolutions in the permittivity of Bi_2Se_3 thin films, and the larger magnitudes for experimental results are due to the excitonic effects involved in the practical experiments but not in the DFT calculations. On the other hand, the decrease of the increment rate in experimental results is more dramatic than that in calculated results, which can be also attributed to the layer-dependent decreasing excitonic effects in the practical Bi_2Se_3 thin films.

The CPs in the permittivity spectra correspond to different inter-band excitations in band structures. We further investigate the physical origins of the optical transitions at the CPs and their evolutions versus the thickness of the Bi_2Se_3 thin film by combining the CP analysis results with the DFT calculations. Fig. 6 summarizes the process for the identification of the optical transitions at the CPs by taking the 2-QL Bi_2Se_3 thin film as an example. As for the 4-QL and 6-QL Bi_2Se_3 thin films, similar results and process can be found in Fig. S6 and Fig. S7. The DFT calculates the band structure along related *k*-branches in the projected Brillouin zone and the partial density of states (PDOS) over the corresponding energy range are shown in Fig. 6(a) and Fig. 6(b), respectively. In Fig. 6(a), V_i and C_i respectively represent the *i*-th highest valance band and the *i*-th lowest conduction band. It can be seen that the calculated surface state gap (0.168 eV) at $\bar{\Gamma}$ is slightly smaller than the experimental value (0.252 eV) [24], because the PBE approximation in the DFT calculations always underestimates bandgap, but the band dispersions (band energy *vs*. momentum space) are reasonable [44,61]. As shown in Fig. 6(b), the PDOS curves indicate that the valance bands below the Fermi level have mostly the Se-4*p* character, but there are also contributions from the Bi-6*s* and Bi-6*p* states, while the conduction bands mostly have the Se-4*p* and Bi-6*p* characters. Fig. 6(c) gives the energy difference ($E_c - E_v$) curves between several valance and conduction bands that are probably involved in the optical transitions over the concerned spectral range. Stationary points on the ($E_c - E_v$) curves, indicating the corresponding valance and conduction bands shown in Fig. 6(a) are basically parallel to each other, correspond to the van Hove singularities in the *k*-space where the gradient $\nabla_k(E_{ck} - E_{vk})$ approaches zero [62]. From the microscopic theory, the imaginary part of permittivity is proportion to the JDOS (J_{cv}) [63]:

$$\varepsilon_i(\omega) \propto J_{cv}(\omega) = \frac{2}{(2\pi)^3} \int_{E_{ck}-E_{vk}=E(\omega)} \frac{dS}{\nabla_k(E_{ck} - E_{vk})}, \tag{4}$$

where S represents the constant energy surface defined by $E_{ck} - E_{vk} = E(\omega)$, and $E(\omega)$ is the energy of the incident light. The van Hove singularities in the JDOS give rise to the CPs in the permittivity. Thus, each CP in the permittivity as shown in Fig. 6(d) can be connected to a specific stationary point in Fig. 6(c).

The transition positions of the CPs in the 2-QL Bi_2Se_3 are demonstrated in Fig. 6(a). Precisely, CP A at 1.27 eV is due to the inter-band transition from V_2 (V_3) to C_2 at the $\bar{\Gamma}$ symmetry point in the projected Brillouin zone, CP B at 1.60 eV involves the transition from V_1 to C_1 at the $\bar{M}$ symmetry point, CP C at 2.09 eV is owing to the inter-band transition from V_2 (V_3) to C_3 at the $\bar{\Gamma}$ symmetry point, CP D at 2.54 eV is due to the promotion of electrons from V_2 (V_3) to C_2 at the $\bar{K}$ symmetry point, and CP E at 3.99 eV contributes from the inter-band transition from V_2 to C_8 at the $\bar{M}$ symmetry point. Moreover, the transitions at all these five CPs are mostly contributed from the Se-4*p* and Bi-6*p* states as demonstrated in Fig. 6(b). As illustrated in Fig. S5, it is clear that as the QL number increases from 2 to 10, the surface state gap decreases from 0.168 eV to 0.013 eV, and the surface state gap nearly disappears at 6 QLs, which agrees with the previous experimental and theoretical results [24,26]. Comparing results of 2–6 QLs in Fig. 6, Fig. S6 and Fig. S7, we elucidate that, as for the 4-QL and 6-QL Bi_2Se_3 thin films, although the surface state gap decreases, the transition positions of A–E CPs are basically the same with those of the 2-QL Bi_2Se_3 thin film. Besides, the approach of the valance and conduction bands at the $\bar{K}$ point explains the proximity phenomenon shown in Fig. 4(b) between CPs C and D with the QL number increasing. In summary of the above results, the transition positions of the CPs in band structures remain virtually unchanged, and the red shifts in the center energies of the CPs shown in Fig. 5(a) are caused by the reduced surface state gap due to the attenuated hybridization of opposite surfaces when the QL increases

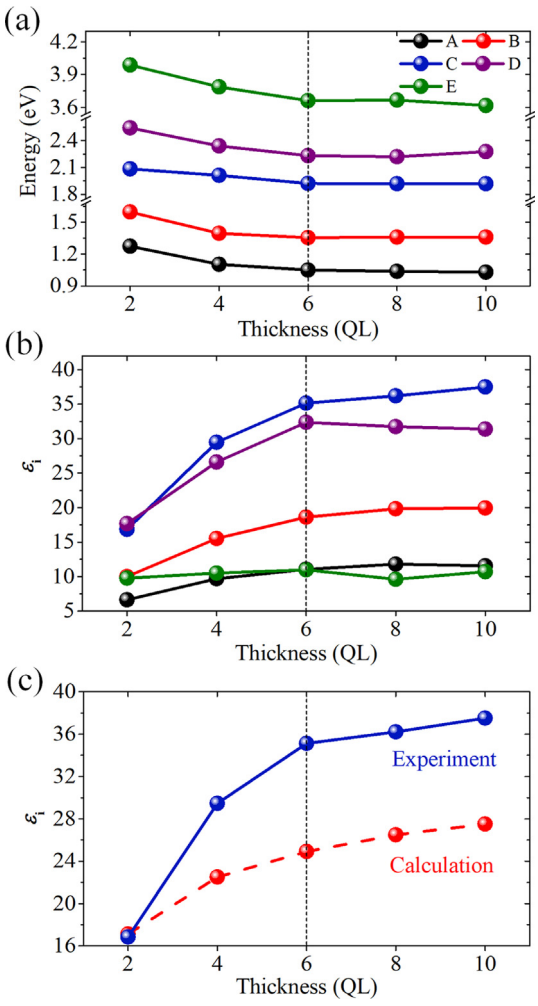

Fig. 5. (a) The central energies of CPs A–E versus the QL number of Bi_2Se_3 thin films. (b) The magnitudes of ε_i at CPs A–E versus the QL number. (c) The experimental and calculated magnitudes of ε_i at CP C versus the QL number.

from 2 to 6.

5. Conclusion

In conclusion, we established a profound study on the layer-dependent evolutions in permittivity of Bi_2Se_3. High-quality, strictly layer-controllable, atomically flat and large area (centimeter-scale) Bi_2Se_3 thin films are successfully prepared by the MBE. Permittivity of 2–10 QL Bi_2Se_3 is evaluated by the SE over an ultra-broad spectral range (0.73–6.43 eV). The ENZ point in the real part of permittivity exhibits a blue shift as the thickness approaches the two-dimensional limit, suggesting the surface plasmon modes could gradually change. The ELF is derived from the permittivity to identify the surface plasmon modes, and ELF peak also exhibits a blue shift as the thickness approaches the two-dimensional limit. These evolutions indicate that the resonance frequencies of surface plasmon modes in Bi_2Se_3 gradually move toward higher energy due to the hybridization-induced surface states gap. Five CPs (A–E) in the permittivity and corresponding optical transitions of these CPs are identified by the CP analysis and DFT calculations. We find that the JDOS dominates the layer-dependent increase in the imaginary part of permittivity at the CPs. Additionally, the transition positions of these CPs are layer-independent, while the CP center energies exhibit red shifts as the QL increases due to the decreasing surface state gap resulted by the attenuated hybridization between the opposite surfaces. The presented basic physical knowledge

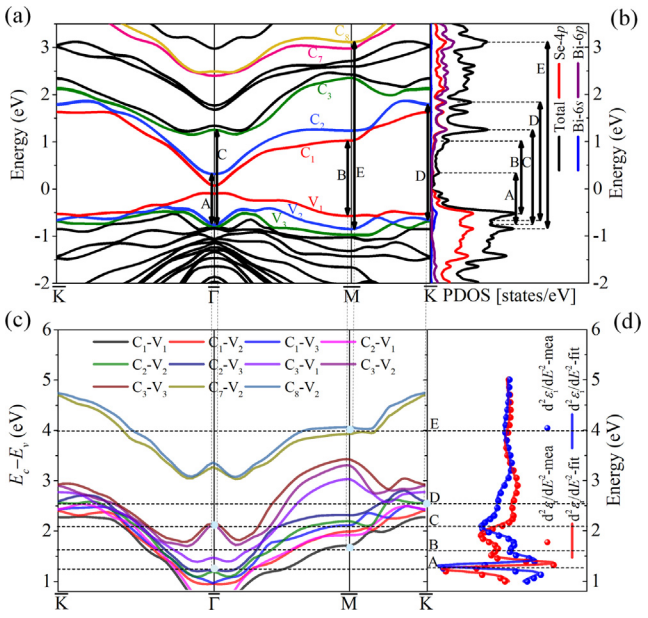

Fig. 6. (a) Band structure of the 2-QL Bi_2Se_3 thin film along relevant *k*-branches in the projected Brillouin zone. (b) PDOS of the 2-QL Bi_2Se_3 thin film in corresponding energy range. The labels A–E in (a) and (b) tag the inter-band transitions corresponding to relevant CPs. (c) Energy difference between valance and conduction band pairs. (d) Second derivative of the permittivity of the 2-QL Bi_2Se_3 thin film. The dots denote the experimental data and lines represent the theoretical fitting. The CPs are labeled with uppercase letters A–E.

of the optical and dielectric properties of Bi_2Se_3 is expected to provide practical guidance and some novel sights for the design of Bi_2Se_3-based electronic and photonic devices.

CRediT authorship contribution statement

Mingsheng Fang: Conceptualization, Methodology, Formal analysis, Investigation, Writing - original draft. **Zhengyu Wang:** Investigation, Resources, Writing - review & editing, Funding acquisition. **Honggang Gu:** Conceptualization, Methodology, Investigation, Writing - original draft, Funding acquisition. **Mingyu Tong:** Resources, Writing - review & editing. **Baokun Song:** Formal analysis, Investigation, Writing - review & editing. **Xiangnan Xie:** Resources, Writing - review & editing. **Tong Zhou:** Resources, Writing - review & editing. **Xiuguo Chen:** Writing - review & editing, Funding acquisition. **Hao Jiang:** Writing - review & editing, Funding acquisition. **Tian Jiang:** Investigation, Resources, Writing - review & editing, Funding acquisition. **Shiyuan Liu:** Conceptualization, Writing - review & editing, Project administration, Funding acquisition.

Declaration of Competing Interest

The authors declare that they have no known competing financial interests or personal relationships that could have appeared to influence the work reported in this paper.

Acknowledgments

We thank Prof. Chao-Yu Chen for helpful discussions. This work was funded by the National Natural Science Foundation of China (Grant No. 51727809, 51805193, 51525502, 51775217), the China Postdoctoral Science Foundation (Grant No. 2017 T100546), the General Program of Beijing Academy of Quantum Information Sciences (Project No. Y18G17), the Scientific Researches Foundation of National University of Defense Technology (Project No. ZK18-01-03), and the National Science and Technology Major Project of China (Grant No. 2017ZX02101006-004). The authors thank the technical support from the Experiment Center for Advanced Manufacturing and Technology in

School of Mechanical Science &Engineering of HUST.

Appendix A. Supplementary material

Supplementary data to this article can be found online at https://doi.org/10.1016/j.apsusc.2019.144822. Additional sample characterizations, detains of the critical point analysis, the DFT calculated surface band gaps and permittivity of 2–10 QL Bi_2Se_3, identification of the optical transitions of the CPs in the 4-QL and 6-QL Bi_2Se_3 thin films can be found in Supplementary Material.

References

[1] M.Z. Hasan, C.L. Kane, Colloquium: topological insulators, Rev. Mod. Phys. 82 (2010) 3045–3067.
[2] C.L. Kane, E.J. Mele, Z_2 topological order and the quantum spin hall effect, Phys. Rev. Lett. 95 (2005) 146802.
[3] B.A. Bernevig, T.L. Hughes, S.C. Zhang, Quantum spin hall effect and topological phase transition in HgTe quantum wells, Science 314 (2006) 1757–1761.
[4] L. Fu, C.L. Kane, E.J. Mele, Topological insulators in three dimensions, Phys. Rev. Lett. 98 (2007) 106803.
[5] A. Politano, V.M. Silkin, I.A. Nechaev, M.S. Vitiello, L. Viti, Z.S. Aliev, M.B. Babanly, G. Chiarello, P.M. Echenique, E.V. Chulkov, Interplay of surface and dirac plasmons in topological insulators: the case of Bi_2Se_3, Phys. Rev. Lett. 115 (2015) 216802.
[6] J. Yin, H.N.S. Krishnamoorthy, G. Adamo, A.M. Dubrovkin, Y. Chong, N.I. Zheludev, C. Soci, Plasmonics of topological insulators at optical frequencies, NGP Asia Mater. 9 (2017) e425.
[7] T.P. Ginley, S. Law, Coupled dirac plasmons in topological insulators, Adv. Optical Mater. 6 (2018) 180013.
[8] J. Qiao, S. Zhao, K. Yang, W.H. Song, W. Qiao, C.L. Wu, J. Zhao, G. Li, D. Li, T. Li, H. Liu, C.K. Lee, High-quality 2-μm Q-switched pulsed solid-state lasers using spin coating-coreduction approach synthesized Bi_2Te_3 topological insulators, Photon. Res. 6 (2018) 314–320.
[9] D. Hsieh, Y. Xia, D. Qian, L. Wray, J.H. Dil, F. Meier, J. Osterwalder, L. Patthey, J.G. Checkelsky, N.P. Ong, A.V. Fedorov, H. Lin, A. Bansil, D. Grauer, Y.S. Hor, R.J. Cava, M.Z. Hasan, A tunable topological insulator in the spin helical Dirac transport regime, Nature 460 (2009) 1101–1105.
[10] J. Linder, Y. Tanaka, T. Yokoyama, A. Sudbø, N. Nagaosa, Unconventional superconductivity on a topological insulator, Phys. Rev. Lett. 104 (2010) 067001.
[11] L. Fu, C.L. Kane, Superconducting proximity effect and majorana fermions at the surface of a topological insulator, Phys. Rev. Lett. 100 (2008) 096407.
[12] F. Wilczek, Majorana returns, Nat. Phys. 5 (2009) 614–618.
[13] J. Lee, Y. Kim, K. Lee, J.H. Lee, Femtosecond mode-locking of a fiber laser using a $CoSb_3$ skutterudite-based saturable absorber, Photon. Res. 6 (2018) C36–C43.
[14] L. Fu, C.L. Kane, Probing neutral majorana fermion edge modes with charge transport, Phys. Rev. Lett. 102 (2009) 216403.
[15] I. Garate, M. Franz, Inverse spin-galvanic effect in the interface between a topological insulator and a ferromagnet, Phys. Rev. Lett. 104 (2010) 146802.
[16] H. Peng, W. Dang, J. Cao, Y. Chen, D. Wu, W. Zheng, H. Li, Z.-X. Shen, Z. Liu, Topological insulator nanostructures for near-infrared transparent flexible electrodes, Nat. Chem. 4 (2012) 281–286.
[17] M.X. Wang, C. Liu, J.P. Xu, F. Yang, L. Miao, M.Y. Yao, C.L. Gao, C. Shen, X. Ma, X. Chen, Z.A. Xu, Y. Liu, S.C. Zhang, D. Qian, J.F. Jia, Q.K. Xue, The Coexistence of superconductivity and topological order in the bi_2se_3 thin films, Science 336 (2010) 52–55.
[18] H. Zhang, C.X. Liu, X.L. Qi, X. Dai, Z. Fang, S.C. Zhang, Topological insulators in Bi_2Se_3, Bi_2Te_3 and Sb_2Te_3 with a single dirac cone on the surface, Nat. Phys. 5 (2009) 438–442.
[19] Y. Xia, D. Qian, D. Hsieh, L. Wray, A. Pal, H. Lin, A. Bansil, D. Grauer, Y.S. Hor, R.J. Cava, M.Z. Hasan, Observation of a large-gap topological-insulator class with a single Dirac cone on the surface, Nat. Phys. 5 (2009) 398–402.
[20] D. Wang, D. Yu, M. Mo, X. Liu, Y. Qian, Preparation and characterization of wire-like Sb_2Se_3 and flake-like Bi_2Se_3 nanocrystals, J. Crystal Growth 253 (2003) 445–451.
[21] L. He, F. Xiu, X. Yu, M. Teague, W. Jiang, Y. Fan, X. Kou, M. Lang, Y. Wang, G. Huang, N.C. Yeh, K.L. Wang, Surface-dominated conduction in a 6 nm thick Bi_2Se_3 thin film, Nano Lett. 12 (2012) 1486–1490.
[22] B. Zhou, H.Z. Lu, R.L. Chu, S.Q. Shen, Q. Niu, Finite size effects on helical edge states in a quantum spin-hall system, Phys. Rev. Lett. 101 (2008) 246807.
[23] Y. Sakamoto, T. Hirahara, H. Miyazaki, S. Kimura, S. Hasegawa, Spectroscopic evidence of a topological quantum phase transition in ultrathin Bi_2Se_3 films, Phys. Rev. B 81 (2010) 165432.
[24] Y. Zhang, K. He, C.Z. Chang, C.L. Song, L.L. Wang, X. Chen, J.F. Jia, Z. Fang, X. Dai, W.Y. Shan, S.Q. Shen, Q. Niu, X.L. Qi, S.C. Zhang, X.C. Ma, Q.K. Xue, Crossover of the three-dimensional topological insulator Bi_2Se_3 to the two-dimensional limit, Nat. Phys. 6 (2010) 584–588.
[25] M. Salehi, H. Shapourian, N. Koirala, M.J. Brahlek, J. Moon, S. Oh, Finite-size and composition-driven topological phase transition in $(Bi_{1-x}In_x)_2Se_3$ thin films, Nano. Lett. 16 (2016) 5528–5532.
[26] Z. Wang, T. Zhou, T. Jiang, H. Sun, Y. Zang, Y. Gong, J. Zhang, M. Tong, X. Xie, Q. Liu, C. Chen, K. He, Q.K. Xue, Dimensional crossover and topological nature of the thin films of a three-dimensional topological insulator by band gap engineering, Nano. Lett. 19 (2019) 4627–4633.
[27] X. Zhang, J. Wang, S.C. Zhang, Topological insulators for high-performance terahertz to infrared applications, Phys. Rev. B 82 (2010) 245107.
[28] F. Giorgianni, E. Chiadroni, A. Rovere, M. Cestelli-Guidi, A. Perucchi, M. Bellaveglia, M. Castellano, D.D. Giovenale, G.D. Pirro, M. Ferrario, R. Pompili, C. Vaccarezza, F. Villa, A. Cianchi, A. Mostacci, M. Petrarca, M. Brahlek, N. Koirala, S. Oh, S. Lupi, Strong nonlinear terahertz response induced by Dirac surface states in Bi_2Se_3 topological insulator, Nat. Commum. 7 (2016) 11421.
[29] F. Wang, L. Li, W. Huang, L. Li, B. Jin, H. Li, T. Zhai, Submillimeter 2D Bi_2Se_3 flakes toward high-performance infrared photodetection at optical communication wavelength, Adv. Funct. Mater. 28 (2018) 1802707.
[30] W. Tang, A. Politano, C. Guo, W. Guo, C. Liu, L. Wang, X. Chen, W. Lu, Ultrasensitive room-temperature terahertz direct detection based on a bismuth selenide topological insulator, Adv. Funct. Mater. 28 (2018) 1801786.
[31] X. Niu, X. Hu, S. Chu, Q. Gong, Epsilon-near-zero photonics: a new platform for integrated devices, Adv. Opt. Mater. 6 (2018) 1701292.
[32] I. Liberal, N. Engheta, Near-zero refractive index photonics, Nat. Photonics 11 (2017) 149–158.
[33] O. Reshef, I.D. Leon, M.Z. Alam, R.W. Boyd, Nonlinear optical effects in epsilon-near-zero media, Nat. Rev. Mater. 4 (2019) 525–551.
[34] M. Zhao, M. Bosman, M. Danesh, M. Zeng, P. Song, Y. Darma, A. Rusydi, H. Lin, C.W. Qiu, K.P. Loh, Visible surface plasmon modes in single Bi_2Te_3 nanoplate, Nano. Lett. 15 (2015) 8331–8335.
[35] H. Gu, B. Song, M. Fang, Y. Hong, X. Chen, H. Jiang, W. Ren, S. Liu, Layer-dependent dielectric and optical properties of centimeter-scale 2D WSe_2: evolution from a single layer to few layers, Nanoscale (2019), https://doi.org/10.1039/c9nr04270a.
[36] S.D. Yang, L. Yang, Y.X. Zheng, W.J. Zhou, M.Y. Gao, S.Y. Wang, R.J. Zhang, L.Y. Chen, Structure-dependent optical properties of self-organized Bi_2Se_3 nanostructures: from nanocrystals to nanoflakes, ACS Appl. Mater. Interfaces 9 (2017) 29295–29301.
[37] P.Y. Yu, M. Cardona, Fundamentals of Semiconductors: physics and materials properties, fourth ed., Springer, Berlin, 2010.
[38] M. Eddrief, F. Vidal, B. Gallas, Optical properties of Bi_2Se_3: from bulk to ultrathin films, J. Phys. D: Appl. Phys. 49 (2016) 505304.
[39] Y.R. Sapkota, A. Alkabsh, A. Walber, H. Samassekou, D. Mazumdar, Optical evidence for blue shift in topological insulator bismuth selenide in the few-layer limit, Appl. Phys. Lett. 110 (2017) 181901.
[40] Z. Li, S. Chen, J. Sun, X. Li, H. Qiu, J. Yang, Spatial and thickness dependence of coupling interaction of surface states and influence on transport and optical properties of few-layer Bi_2Se_3, J. Phys.: Condens. Matter. 30 (2018) 065503.
[41] J. Zhang, T. Jiang, T. Zhou, H. Ouyang, C. Zhang, Z. Xin, Z. Wang, X. Cheng, Saturated absorption of different layered Bi_2Se_3 films in the resonance zone, Photon. Res. 6 (2018) C8–C14.
[42] R. Wyckoff, Crystal Structures, second ed., Interscience Publishers, New York, 1960.
[43] J.P. Perdew, K. Burke, M. Ernzerhof, Generalized Gradient Approximation Made Simple, Phys. Rev. Lett. 77 (1996) 3865–3868.
[44] W. Liu, X. Peng, X. Wei, H. Yang, G.M. Stocks, J. Zhong, Surface and substrate induced effects on thin films of the topological insulators Bi_2Se_3 and Bi_2Te_3, Phys. Rev. B 87 (2013) 205315.
[45] K.M.F. Shahil, M.Z. Hossain, V. Goyal, A.A. Balandin, Micro-Raman spectroscopy of mechanically exfoliated few-quintuple layers of Bi_2Te_3, Bi_2Se_3, and Sb_2Te_3 materials, J. App. Phys. 111 (2012) 054305.
[46] S. Liu, X. Chen, C. Zhang, Development of a broadband Mueller matrix ellipsometer as a powerful tool for nanostructure metrology, Thin Solid Films 584 (2015) 176–185.
[47] H. Gu, X. Chen, H. Jiang, C. Zhang, S. Liu, Optimal broadband Mueller matrix ellipsometer using multi-waveplates with flexibly oriented axes, J. Opt. 18 (2016) 025702.
[48] B. Song, H. Gu, S. Zhu, H. Jiang, X. Chen, C. Zhang, S. Liu, Broadband optical properties of graphene and HOPG investigated by spectroscopic Mueller matrix ellipsometry, Appl. Surf. Sci. 439 (2018) 1079–1087.
[49] B. Song, H. Gu, M. Fang, Y.-T. Ho, X. Chen, H. Jiang, S. Liu, Complex optical conductivity of two-dimensional MoS_2: a striking layer dependency, J. Phys. Chem. Lett. 10 (2019) 6246–6252.
[50] H. Fujiwara, Spectroscopic Ellipsometry: Principles and Applications, John Wiley & Sons, Chichester, West Sussex, England, 2007.
[51] A.S. Ferlauto, G.M. Ferreira, J.M. Pearce, C.R. Wronski, R.W. Collinsa, X. Deng, G. Ganguly, Analytical model for the optical functions of amorphous semiconductors from the nearinfrared to ultraviolet: Applications in thin film photovoltaics, J. Appl. Phys. 92 (2002) 2424–2436.
[52] R.A. Synowicki, T.E. Tiwald, Optical properties of bulk c-ZrO_2, c-MgO and a-As_2S_3 determined by variable angle spectroscopic ellipsometry, Thin solid films 455–456 (2004) 248–255.
[53] S.A. Maier, Plasmonics: fundamentals and applications, Springer, New York, 2007.
[54] J.Y. Ou, J.K. So, G. Adamo, A. Sulaev, L. Wang, N.I. Zheludev, Ultraviolet and visible range plasmonics in the topological insulator $Bi_{1.5}Sb_{0.5}Te_{1.8}Se_{1.2}$, Nat. Commun. 5 (2014) 5139.
[55] N. Talebi, C. Ozsoy-Keskinbora, H.M. Benia, K. Kern, C.T. Koch, P.A.V. Aken, Wedge dyakonov waves and dyakonov plasmons in topological insulator Bi_2Se_3 probed by electron beams, ACS Nano. 10 (2016) 6988–6994.
[56] T. Stauber, Plasmonics in Dirac systems: from graphene to topological insulators, J. Phys.: Condens. Matter 26 (2014) 123201.
[57] Y. Yu, Y. Yu, Y. Cai, W. Li, A. Gurarslan, H. Peelaers, D.E. Aspnes, C.G.V.d. Walle, N.V. Nguyen, Y.W. Zhang, L. Cao, Exciton-dominated dielectric function of atomically thin MoS_2 films, Sci. Rep. 5 (2015) 16996.

[58] C. Weisbuch, B. Vinter, Quantum Semiconductor Structures: Fundamentals and applications, Academic Press, San Diego, 1991.
[59] B. Song, H. Gu, M. Fang, X. Chen, H. Jiang, R. Wang, T. Zhai, Y.T. Ho, S. Liu, Layer-dependent dielectric function of wafer-scale 2D MoS_2, Adv. Optical Mater. (2018) 1801250.
[60] H. Shi, H. Pan, Y.W. Zhang, B.I. Yakobson, Quasiparticle band structures and optical properties of strained monolayer MoS_2 andWS_2, Phys. Rev. B 87 (2013) 155304.
[61] O.V. Yazyev, J.E. Moore, S.G. Louie, Spin Polarization and Transport of Surface States in the Topological Insulators Bi_2Se_3 and Bi_2Te_3 from First Principles, Phys. Rev. Lett. 105 (2010) 266806.
[62] A.M.A. Leguy, P. Azarhoosh, M.I. Alonso, M. Campoy-Quiles, O.J. Weber, J. Yao, D. Bryant, M.T. Weller, J. Nelson, A. Walsh, M.v. Schilfgaarde, P.R.F. Barnes, Experimental and theoretical optical properties of methylammonium lead halide perovskites, Nanoscale 863 (2016) 17–6327.
[63] M.I. Alonso, M. Garriga, Optical Properties of Semiconductors, in: H. Fujiwara, R.W. Collins (Eds.), Spectroscopic Ellipsometry for Photovoltaics, Springer, Cham, 2018, pp. 89–113.

Supplementary data

Layer-dependent dielectric permittivity of topological insulator Bi_2Se_3 thin films

Mingsheng Fang[1], Zhenyu Wang[3,4], Honggang Gu[1,*], Mingyu Tong[2], Baokun Song[1], Xiangnan Xie[5], Tong Zhou[5], Xiuguo Chen[1], Hao Jiang[1], Tian Jiang[2,*], Shiyuan Liu[1,*]

[1]*State Key Laboratory of Digital Manufacturing Equipment and Technology, Huazhong University of Science & Technology, Wuhan 430074, China.*

[2] *College of Advanced Interdisciplinary Studies, National University of Defense Technology, Changsha 410073, P. R. China*

[3] *National Innovation Institute of Defense Technology, Academy of Military Sciences PLA China, Beijing 100010, P. R. China*

[4] *Beijing Academy of Quantum Information Sciences, Beijing 100084, P. R. China*

[5] *State Key Laboratory of High Performance Computing, College of Computer, National University of Defense Technology, Changsha 410073, P. R. China*

*Corresponding authors: *hongganggu@hust.edu.cn; tjiang@nudt.edu.cn; shyliu@hust.edu.cn*

Optical micrograph and AFM

The surface conditions of high quality Bi_2Se_3 thin films were checked by an optical microscope (OM). As showed in Fig. S1, the Bi_2Se_3 thin films has a large area of smooth surface, which is fit to perform ellipsometric measurements. The surface roughness and thicknesses of the Bi_2Se_3 thin films (4 QLs, 8 QLs and 10 QLs) were measured by AFM, as illustrated in Fig. S2. The scanned area in the AFM measurements is 1 μm ×1 μm. (*R*q represents the root-mean-square roughness).

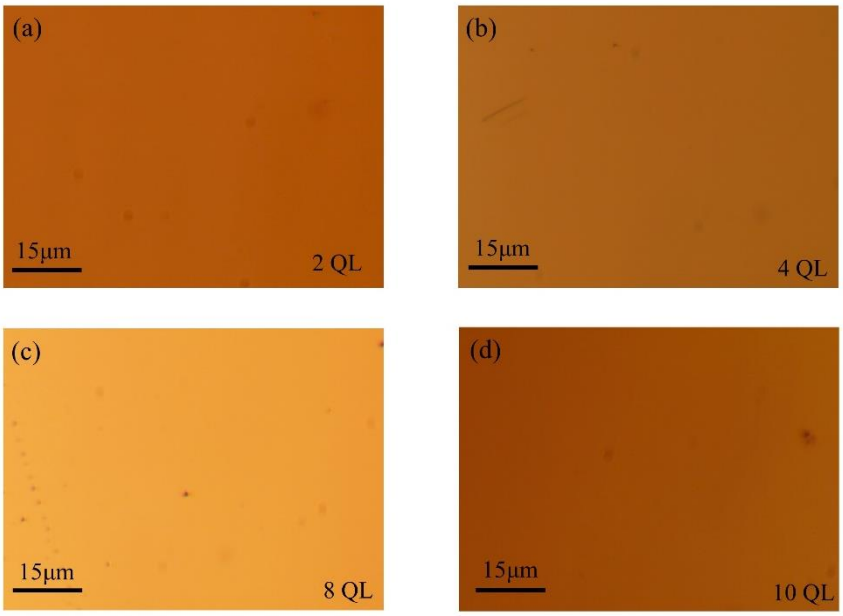

Fig. S1. Optical micrographs of the Bi_2Se_3 thin films

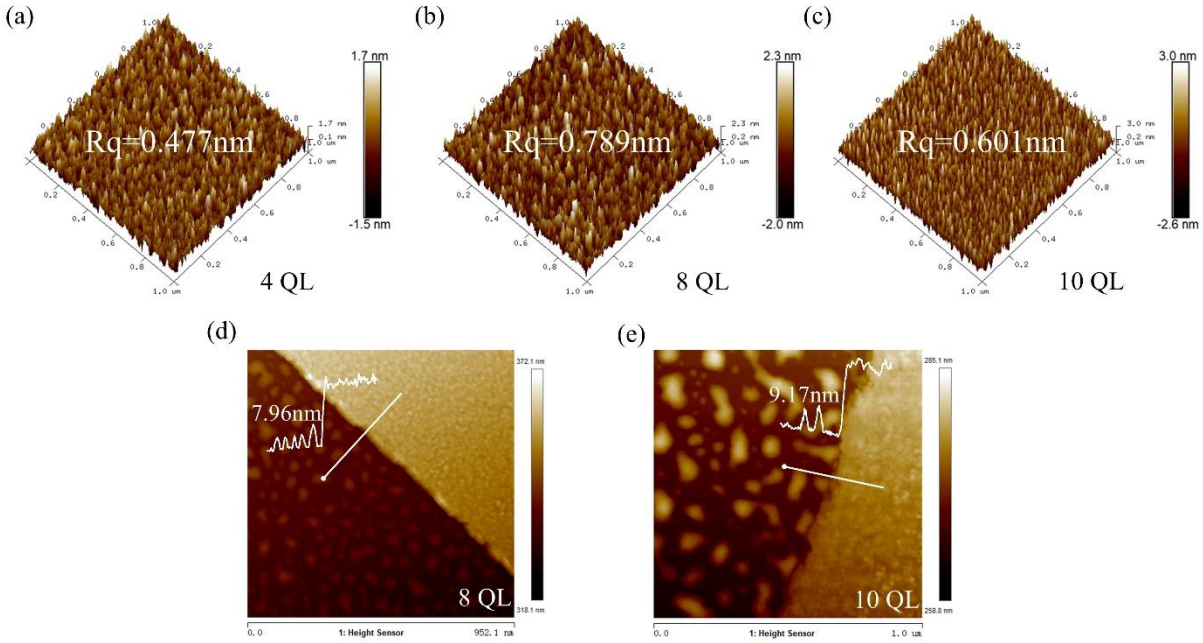

Fig. S2. AFM results of the Bi_2Se_3 thin films

Theoretical and experimental thicknesses of the Bi_2Se_3 thin films

We summarize the theoretical thickness and the SE, AFM and HRTEM measured experimental thicknesses of the Bi_2Se_3 thin films in Table S1.

Table S1. A summary of theoretical and experimental thicknesses of the Bi_2Se_3 thin films.

QL number		2 QL	4 QL	6 QL	8 QL	10 QL
Thickness (nm)	Theory	1.90	3.80	5.70	7.60	9.50
	SE	1.97	3.82	5.61	7.87	9.22
	AFM		3.73		7.96	9.17
	HRTEM		3.86			

Critical point (CP) analysis

In the critical point analysis, the second derivative of dielectric permittivity with respect to photon energy is fitting by the following formulas [1]:

$$\frac{d^2\varepsilon}{dE^2} = \begin{cases} n(n-1)Ae^{i\phi}(E-E_0+i\Gamma)^{n-2}, & n \neq 0 \\ Ae^{i\phi}(E-E_0+i\Gamma)^{-2}, & n = 0 \end{cases} \quad \text{(S1)}$$

where A is the amplitude, ϕ is phase angle, E_0 is the center energy, Γ is the broadening of the peak. n is the dimensionality of the CPs depending on the band structure, three-dimensional CP corresponds to n = 1/2, n = 0 for two-dimensional CP, n = –1/2 for one-dimensional CP and –1 for excitonic CP. The $d^2\varepsilon/dE^2$ of the Bi_2Se_3 thin films was best fit by CPs corresponding to excitonic ones (n = –1). The fitting curves were presented in Fig. S3 and the parameters corresponding to the fitting results are shown in Table S2.

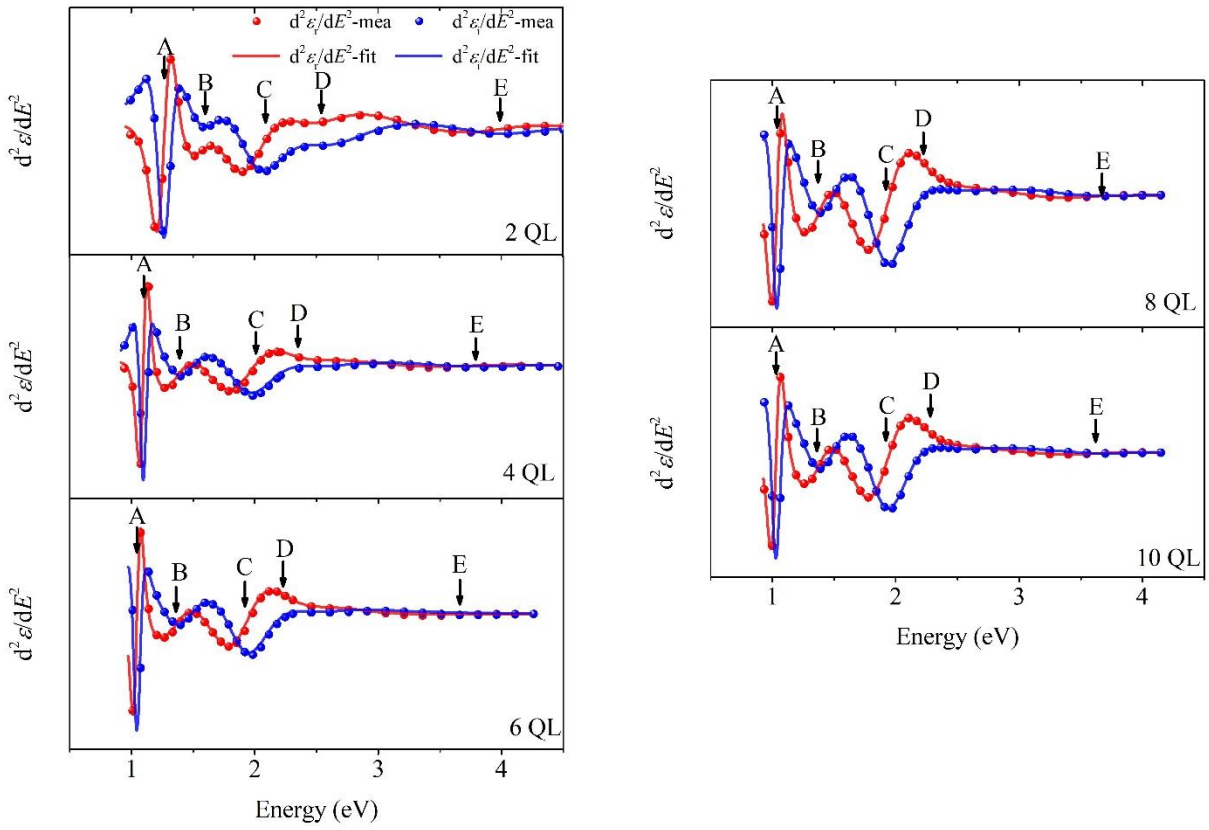

Fig. S3. The measured and the best fitting $d^2\varepsilon/dE^2$ spectra of the Bi_2Se_3 thin films. The experimental data is represented by the solid points, while the fit is represented by the solid lines.

Table S2. Best fitting parameters of the CPs analysis for the Bi_2Se_3 thin films.

Parameters	CPs	2 QL	4 QL	6 QL	8 QL	10 QL
Amp	A	0.23	0.15	0.16	0.29	0.28
(F/m)	B	5.03	2.69	3.69	4.12	3.86

	C	4.30	14.85	11.73	13.92	16.27
	D	4.04	7.91	4.33	6.07	8.45
	E	1.79	3.09	1.10	1.02	1.30
Phase (°)	A	122.68	153.96	147.60	191.52	185.25
	B	109.41	160.14	122.01	122.10	109.64
	C	158.85	147.45	172.44	134.86	109.84
	D	134.68	59.95	128.25	146.19	190.07
	E	141.78	134.75	152.46	139.68	127.71
Central Energy (eV)	A	1.27	1.10	1.05	1.04	1.03
	B	1.60	1.39	1.36	1.36	1.36
	C	2.09	2.01	1.92	1.92	1.92
	D	2.54	2.34	2.23	2.22	2.28
	E	3.99	3.79	3.66	3.67	3.62
Broadening (eV)	A	0.15	0.08	0.08	0.11	0.10
	B	0.57	0.36	0.38	0.38	0.36
	C	0.49	0.54	0.46	0.45	0.50
	D	0.72	0.67	0.62	0.60	0.59
	E	0.82	0.87	0.71	0.62	0.68

Density function theory (DFT) calculated results

Dielectric permittivity of thin Bi_2Se_3 films using DFT methods without involving excitonic effects was calculated, as shown in Fig. S4. Besides, the calculated surface state gaps from 2-QL to 10-QL Bi_2Se_3 thin films were illustrated in Fig. S5.

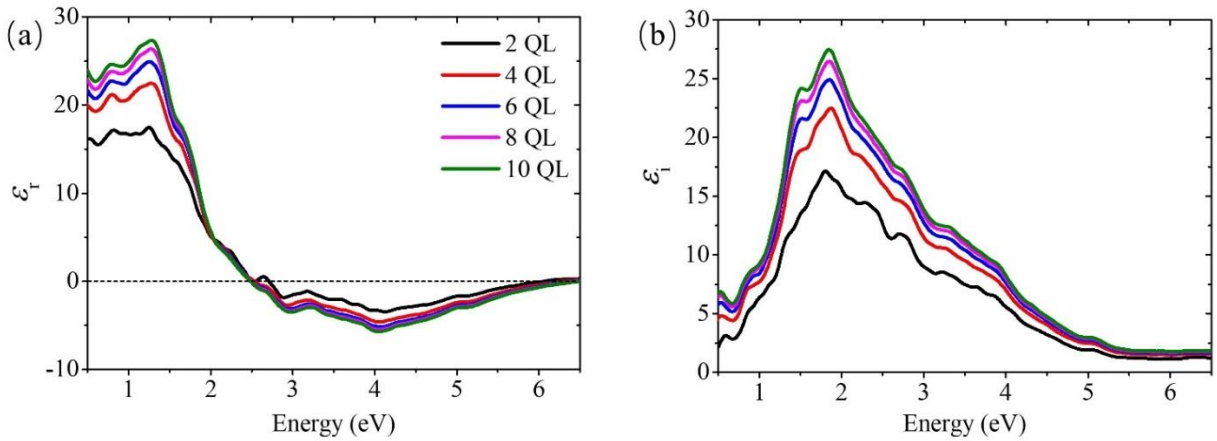

Fig. S4. The calculated dielectric permittivity of 2–10 QL Bi_2Se_3 thin films. (a) Real part. (b) Imaginary part.

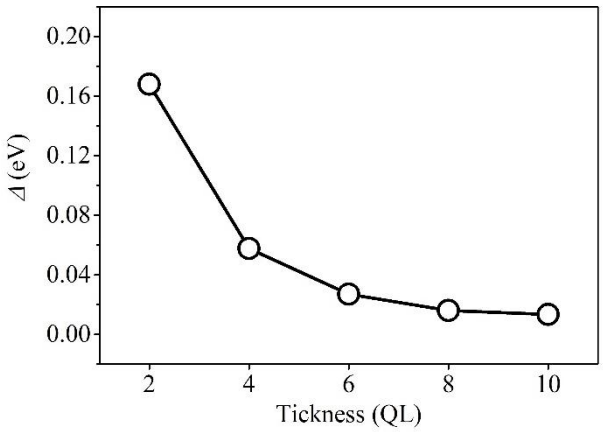

Fig. S5. The calculated surface state gaps of Bi_2Se_3 thin films with different thickness.

The interband transitions in 4-QL and 6-QL Bi_2Se_3 thin films

The inter-band excitations in band structures and PDOS corresponding to the five critical points (CPs) in 4-QL and 6-QL Bi_2Se_3 thin films are shown in Fig. S6 and Fig. S7.

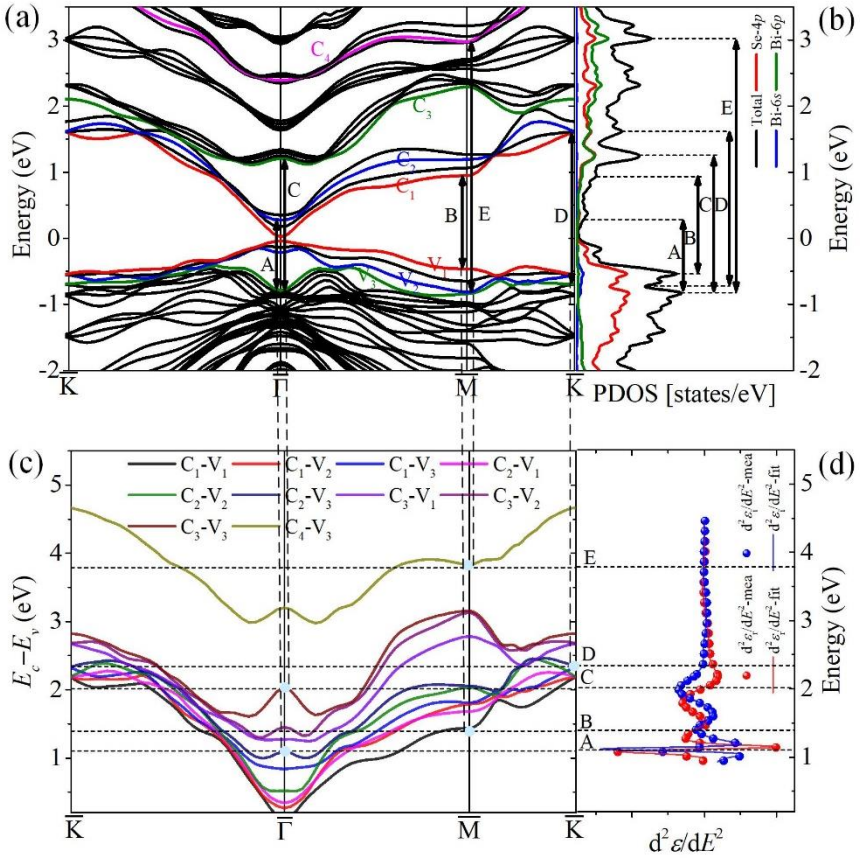

Fig. S6. The analysis results in 4-QL Bi_2Se_3 thin films

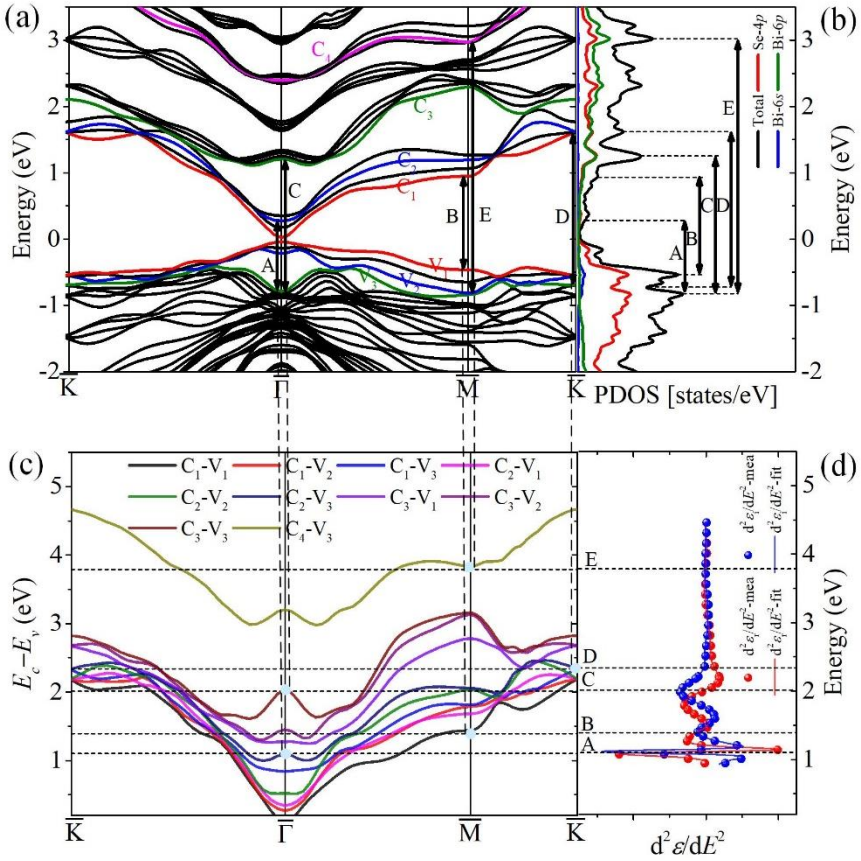

Fig. S7. The analysis results in 6-QL Bi_2Se_3 thin films

References

[1] P. Lautenschlager, M. Garriga, L. Vina, M. Cardona, Temperature dependence of the dielectric function and interband critical points in silicon, Phys. Rev. B. 36 (1987) 4821.